ACS OMEGA

Article

Cite This: ACS Omega 2019, 4, 17223−17229

http://pubs.acs.org/journal/acsodf

# CMOS-Compatible Titanium Nitride for On-Chip Plasmonic Schottky Photodetectors

Jacek Gosciniak,*[,†] Fatih B. Atar,[‡] Brian Corbett,[‡] and Mahmoud Rasras[†]

[†]New York University Abu Dhabi, Saadiyat Island, Abu Dhabi, UAE

[‡]Tyndall National Institute, Lee Malting Point, Cork T12 R5CP, Ireland

**ABSTRACT:** Here, we propose a waveguide-integrated plasmonic Schottky photodetector (PD) operating based on an internal photoemission process with a titanium nitride plasmonic material. The theoretically examined structure employs an asymmetric metal−semiconductor−metal waveguide configuration with one of the electrodes being gold and the second being either gold, titanium, or titanium nitride. For the first time, we measured a Schottky barrier height of 0.67 eV for titanium nitride on p-doped silicon, which is very close to the optimal value of 0.697 eV. This barrier height will enable photodetection with a high signal-to-noise ratio when operating at a wavelength of 1550 nm. In addition to the measured optical properties of high absorption losses and reasonably large real part of the permittivity that are desired for this type of PD, titanium nitride is also compatible with easy integration on existing complementary metal−oxide−semiconductor technology. The use of titanium nitride results in a shorter penetration depth of the optical mode into the metal when compared to Ti, which in turn enhances the probability for transmission of hot electrons to the adjacent semiconductor, giving rise to an enhancement in responsivity.

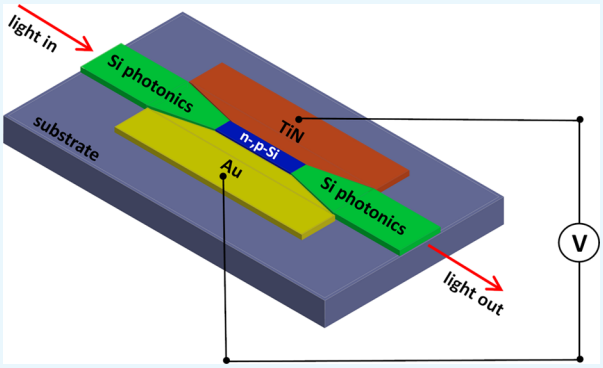


## INTRODUCTION

Photodetectors (PDs) are one of the basic building blocks of an optoelectronic link that converts light into an electrical signal. On-chip monolithic optoelectronic integration requires the development of complementary metal−oxide−semiconductor (CMOS)-compatible PDs that operate in the telecom wavelengths (1.1−1.7 $\mu$m).[1−3] While sensitivity is the most important attribute for PDs in long-distance communications, for short-distance interconnects, the most critical factor is the total energy dissipated per bit. The optical energy received at the PD is directly related to the transmitter optical output power and the total link loss, which includes the coupling losses, the link attenuation, and additionally, a power margin. Hence, for 10 fJ/bit transmitted optical energy, the received optical energy could be 1 fJ/bit.[3] Thus, minimizing the optical losses at the PD is crucial for optimizing the performance of the overall system.

PDs usually operate on the basis of the photoelectric effect or exhibit an electrical resistance dependent on the incident radiation. The principle is based on the absorption of photons and the subsequent separation of the photogenerated charge carriers—electron−hole (e−h) pairs.[4] However, this approach does not work for near-infrared (NIR) light in Si because the NIR photon energies (0.79−0.95 eV) have no sufficient energy to overcome the Si band gap (1.12 eV). In the case of Ge-based PDs (band gap 0.67 eV), the small PD detection area limits the response.[4] An alternative approach utilizes the intrinsic absorption of the metal for photodetection that is accomplished by internal photoemission (IPE) in a Schottky diode.[5−10] In this configuration, the photoexcited ("hot") carriers in the metal are emitted to the semiconductor/insulator over a potential $\Phi_B$, called the Schottky barrier, that exists at the metal−semiconductor (MS) interface.

In the semiconductor/insulator, the injected carriers are accelerated by the electric field present in the depletion region of the Schottky diode and then collected as a photocurrent at the external electrical contacts. Usually, the Schottky barrier is lower than the band gaps of most semiconductors, thus allowing photodetection of NIR photons with energy $h\nu > \Phi_B$. The process of photon-induced emission of electrons from metals and its collection was described by Spicer.[11,12] It is based on the Fowler proposal and consists of a three-step model: (1) generation of hot electrons in the metal through the absorption of photons, (2) diffusion of a portion of the hot electrons to the MS/insulator interface before thermalization, and (3) injection of the hot electrons with sufficient energy and correct momentum into the conduction band of the semiconductor/insulator through IPE.

To optimize the efficiency of the IPE process, the optical power should be confined at the boundary between the materials forming the Schottky barrier. This allows for an increased interaction of the light with the metal in a very close

Received: June 10, 2019
Accepted: September 20, 2019
Published: October 7, 2019

vicinity of the interface where the photoemission process takes place. The solution for this is well known and is called a surface plasmon polariton (SPP). The SPPs are guided optical surface waves propagating along the boundary between the metal and dielectric with a maximum field located at this interface and decaying exponentially in both media.[13,14] One of the main advantages of SPP emanates from the fact that it is not diffraction-limited while tightly confining the optical field to deep subwavelength dimensions. SPP offers a long interaction length between the propagating mode and the PD, and therefore, a larger portion of the optical energy can be absorbed adjacent to the Schottky barrier from where it is collected.

Plasmonic elements including PDs have been suggested as an alternative technology to overcome the scaling limitations of conventional photonic components.[15] They offer high integration densities, low device capacitance for higher bandwidth operation, and operation with ultralow energies. SPPs can decay either radiatively via emission of photons or nonradiatively through the generation of excited (hot) carriers. The photoexcited hot carriers with sufficient energy have the possibility to overcome the potential barrier between the metal and the semiconductor, leading to a measurable current through light-induced charge separation. The potential barrier can be overcome either directly by the high-energy electrons or through quantum mechanical tunneling. The probability of tunneling depends on the barrier width and height as well as the charge carrier energy.

## RESULTS AND DISCUSSION

The considered arrangement consists of a metal−semiconductor−metal (MSM) structure with the semiconductor Si placed between the metals (see Figure 1), similar to the one

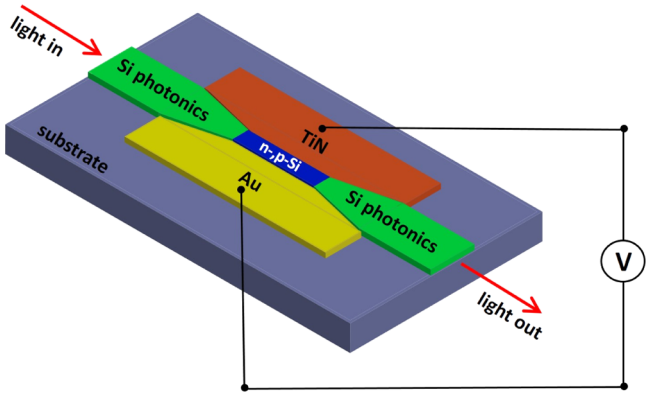


**Figure 1.** Schematic of the asymmetric MSM waveguide structure implemented for photodetection with the light coupled from the Si waveguide to the MSM junction, which is biased with an external voltage.

presented in ref 5. For this plasmonic waveguide structure, the electric field of the propagating mode reaches maxima at both MS interfaces and decays exponentially into the semiconductor, with the electromagnetic energy distributed across the metal and semiconductor. The relative amount of energy in the metal and the semiconductor depends on the optical properties of the material and the waveguiding geometry. The penetration depth of light into the metal, that is, the skin depth, depends on the optical properties of the metal.[13,14] A large negative real part of the permittivity, which is a consequence of large plasma frequency because of larger carrier concentration, gives rise to a small penetration of the field into the metal, whereas a small imaginary part of the permittivity leads to lower absorption in the metal.[13,14] Therefore, it can be deduced that the field penetration into the metal influences the trade-off between confinement and propagation losses—that is, less light in the metal results in more inside the dielectric what lowers the absorption losses and confinement of the mode.

Here, we examine TiN as a replacement for Ti as it shows much better plasmonic behavior and, consequently, is able to confine the absorbed energy much closer to the MS interface. As a result, the hot carriers have much higher probability to be transferred across the Schottky barrier. The probability of hot carrier transfer increases significantly for metals with low Fermi level. To calculate the probability of hot electron injection to the semiconductor over the potential barrier requires finding a relation between the lateral wavevector, $k_{\|m}$, which is continuous across the boundary, and the wavevectors, $k_{zm}$ and $k_{zs}$, that is, the wavevectors in the metal and semiconductor, respectively, that are normal to the interface[30]

$$k_{zm} = \sqrt{{k_F}^2 - {k_{\|m}}^2}$$

$$k_{zs} = \sqrt{{k_{max}}^2 - {k_{\|m}}^2}$$

$${k_{max}}^2(E) = \frac{2m_s}{\hbar^2}(E - \phi_B) = \frac{m_s E - \phi_B}{m_0 E_F}{k_F}^2$$

Here, $E_F = \hbar^2 {k_F}^2/2m_0$ is the Fermi energy, $k_F$ is the Fermi wavevector, $m_0$ is the mass of the electron in the metal, and $m_s$ is the effective mass of the electron in the semiconductor. Only the hot electrons with the lateral wavevector, $k_{\|m}$, less than $k_{max}$, have a finite probability to be transferred over the Schottky barrier. The hot electrons which can be injected into the semiconductor have a cone of allowed wavevectors given by $\sin^2\theta = {k_{max}}^2/{k_F}^2$. Inside the cone, the probability of IPE of a hot electron that is generated by a photon with energy $\hbar\omega$ is given by[30]

$$T_0(\hbar\omega) = \frac{m_s\hbar\omega - \phi_B}{m_0 E_F}$$

Among many metals commonly used in plasmonics, TiN possesses the lowest Fermi energy ($E_F$ = 4.2 eV) that makes it favorable for this type of photodetection. Furthermore, good plasmonic properties comparable with that of Au make TiN an ideal candidate as a replacement for Au and development of CMOS-compatible PDs.

The operation principle is based on the intrinsic absorption of metals that is accomplished by IPE.[5−10] The absorbed photons in the metal create hot carriers that are transmitted across a potential barrier at the MS interface. Plasmonics is an ideal approach for realizing such PDs as a metal stripe can be used both to act as an electrode and to support the plasmonic mode, with the mode field strongly localized at the MS interface where it reaches its maximum. Thus, light is perfectly concentrated in the region where its absorption leads to the highest generation rate of photoelectrons. To minimize the dark current in the presented MSM configuration, one of the metal electrodes needs to act more as an absorbent compared to the other. Hence, an asymmetric MSM structure is highly



DOI: 10.1021/acsomega.9b01705
ACS Omega 2019, 4, 17223−17229

desired, where the light is mostly absorbed in one MS interface.

The band diagram of an asymmetric MSM, Au−Si−TiN, PD junction is sketched in Figure 2 with the plasmonic mode

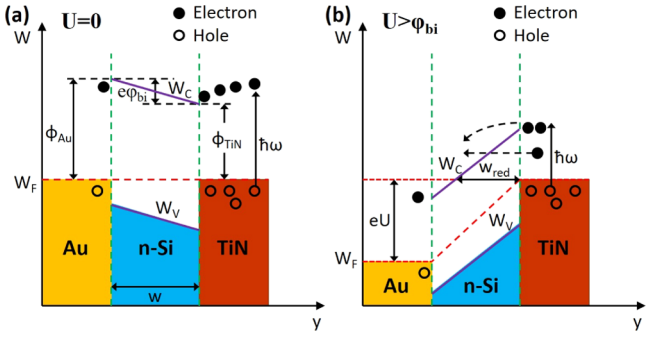


**Figure 2.** Energy band diagram of the Au−Si−TiN junction with (a) no bias voltage (thermal equilibrium) and (b) under an applied forward bias voltage $V$, being positive in the Au → TiN direction.

guided between the metal contacts (Figure 1). In this junction, the SPP mode mostly dissipates its energy at the Si−TiN interface where hot electrons are created in the TiN metal by the absorbed photons.[22−25] When the maximum carrier energies exceed the Fermi energy, the hot electrons have an increased probability of crossing the potential barrier at the TiN−Si interface. Also, if the Schottky barrier height at the second MS interface (Au−Si) exceeds that of the TiN−Si interface, the built-in potential difference $\varphi_{bi}$ across the silicon core impedes electron photoemission. Therefore, no significant current flow can be observed. For an applied voltage to the Au−TiN electrodes, when a positive potential at the Au electrode exceeds $\varphi_{bi}$, the photoemission from TiN is enabled.

In this paper, we examine the impact of different metal materials such as gold (Au), titanium (Ti), and titanium nitride (TiN) on the performances of the PD. Gold has been the metal of choice for most plasmonic components.[13,14] However, it has a relatively low melting temperature, low mechanical durability, high surface energies, and incompatibility with standard CMOS fabrication.[16,17] These major drawbacks have limited its commercial uptake in many potential applications. In contrast, Ti and TiN are CMOS-compatible and are characterized by high melting temperature, extreme mechanical durability, and low surface energy.[16] Furthermore, TiN shows optical properties similar to those of gold, which makes it attractive for many applications.[16−19] In our MSM PD arrangement, the left electrode is chosen to be Au, while the second electrode changes between Au (symmetric MSM)[25] and Ti and TiN (asymmetric MSM).[26]

For the optical characterization, thin 100 nm-thick films of TiN were deposited on the $SiO_2$ substrate by dc reactive magnetron sputtering from a 99.99% titanium target in an argon−nitrogen environment. To achieve a "metallic" TiN, the deposition rate and substrate temperature were kept constant at 1.38 nm/min and 150 °C, respectively. After deposition, the optical constants of the TiN films were extracted from variable angle spectroscopic ellipsometry measurements performed at room temperature over a spectral range of 400−1700 nm with the dielectric functions fitted to the Drude−Lorentz model. By slightly changing the deposition rate and substrate temperature, the TiN optical properties can be tuned.[18,19] Finally, the dielectric functions were compared with gold and titanium. As observed, Au shows the highest negative real part of permittivity, while the imaginary part is the lowest among the presented materials. In comparison, Ti shows a very small negative real part of permittivity, while the imaginary part is higher compared to that of Au. In the case of TiN, it shows a similar real part as Au, while the imaginary part of permittivity for sample TiN 2018 is higher for longer wavelengths compared to that for sample TiN 2014.[18,19] It is a consequence of slightly higher oxygen incorporation during a fabrication process.

To characterize the electrical properties of TiN−Si contacts, we measured the current−voltage ($I$−$V$) characteristics for TiN deposited on both n-doped ($n$ = 2−4 Ω·cm) and p-doped ($n$ = 10−20 Ω·cm) silicon. The TiN thickness was $h$ = 50 nm for both samples for which a sheet resistance was measured at 50 Ω/sq. ($\rho = 2.5 \times 10^4$ Ω·cm), while its diameter changed from $d$ = 100 $\mu$m to $d$ = 200 $\mu$m. A ring-shaped Au structure was used as the top contact on the TiN/p-Si device. The substrate was used as the bottom contact (inset in Figure 3b).

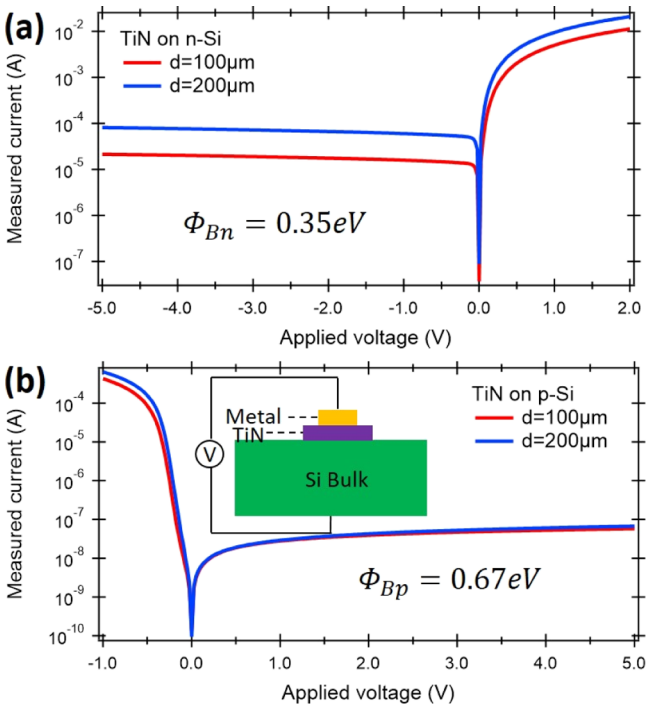


**Figure 3.** Measured current−voltage ($I$−$V$) characteristics of the fabricated TiN−Si junction (inset in b) for different TiN contact areas—diameter $d$ = 100 $\mu$m and $d$ = 200 $\mu$m. Schottky barrier heights of $\Phi_B$ = 0.35 eV and $\Phi_B$ = 0.67 eV for (a) n-doped and (b) p-doped Si, respectively.

For a Schottky PD, the barrier height is a very important parameter. Values for the barrier heights of Au and Ti were taken from the literature,[5,7,20] while for TiN, its value was extracted from our $I$−$V$ measurements (Figure 3). The dark current of a Schottky diode is expressed by

$$I = SA^*T^2 \exp\left(\frac{e\Phi_B}{kT}\right)\left[\exp\left(\frac{eV}{kT}\right) - 1\right]$$

where $S$ is the contact area, $A^*$ is the effective Richardson constant, $\Phi_B$ is the Schottky barrier height, and $V$ is the applied voltage.



DOI: 10.1021/acsomega.9b01705
ACS Omega 2019, 4, 17223−17229

As can be observed from Figure 3, the smaller contact area results in a smaller dark current. However, this behavior is more pronounced for TiN on n-doped Si (Figure 3a) because of the lower Schottky barrier height when compared to that for TiN on p-doped Si as more carriers can flow from TiN to Si. For TiN−p-Si (Figure 3b), the device shows a rectifying behavior with the forward bias current limited by the series resistance of the contact ($R_S$ = 822 Ω). The dark current of 8.1 nA was measured for a reverse bias of 0.1 V. The ideality factor was calculated to be $n$ = 1.3. For the TiN−n-Si contact (Figure 3a), the series resistance of the contact was calculated to be $R_S$ = 110 Ω, while the dark current was around 0.46 μA for a bias voltage of −0.1 V. The ideality factor was calculated to be 1.3. The Schottky barriers deducted from the curves were $\Phi_{TiN}$ = 0.35 eV for n-Si and $\Phi_{TiN}$ = 0.67 eV for p-Si. The inset in Figure 3b shows the measurement setup.

The barrier heights for Au on n-Si- and p-Si-type substrates were taken at $\Phi_{Au}$ = 0.8 eV and $\Phi_{Au}$ = 0.32 eV, respectively, while those for Ti were taken at $\Phi_{Ti}$ = 0.5 eV for n-Si and $\Phi_{Ti}$ = 0.61 eV for p-Si.

Thus, for the n-Si core-based MSM structure, the calculated, established built-in potential differences across the core are $\varphi_{bi}$ = 0.3 eV and $\varphi_{bi}$ = 0.45 eV for Au−Si−Ti and Au−Si−TiN, respectively. For p-doped Si, the corresponding potential difference is $\varphi_{bi}$ = −0.29 eV for Au−Si−Ti and $\varphi_{bi}$ = −0.35 eV for Au−Si−TiN. A negative potential sign means a lower Schottky barrier at the Au interface compared to the second interface—Ti−Si or TiN−Si. It should be mentioned here that the Schottky barrier height between Au and p-doped Si differs greatly from the data presented in ref 5 where the Schottky barrier height was taken as $\Phi_{Au}$ = 0.82 eV. However, even references provided in this paper suggest that this value refers to n-doped Si rather than p-Si.[21] Consequently, the built-in potential difference of $\varphi_{bi}$ = 0.2 eV in Au−(p-Si)−Ti used in the literature[5] is not proper. However, the presented results constitute an excellent step in the realization of future waveguide-integrated PDs.

When light is coupled to the MSM plasmonic waveguide, it dissipates its energy at both MS interfaces. The amount of power absorbed at a given interface depends on the metal's optical properties—the larger the magnitude of the imaginary part of the complex permittivity, the larger the absorption. The device geometry was simulated for 1550 nm appropriate to telecom application by using the two-dimensional finite element method (FEM) with COMSOL. The FEM is a well-established technique for the numerical solution of partial differential equations or integral equations, where the region of interest is subdivided into small segments and the partial differential equation is replaced with a corresponding functional. In our calculations, the complex permittivities of Au, Ti, and TiN[18,19] were taken at the wavelength of 1550 nm.[18,19] As the probability of hot electron transfer to a semiconductor depends strongly on the position in the metal where the electrons are generated, the penetration depths of the SPP electric field in the metal $d_m$ should be considered. The penetration depth can be expressed by

$$d_m = \frac{\lambda}{2\pi}\sqrt{-\frac{\varepsilon_m' + \varepsilon_d}{\varepsilon_m'^2}}$$

where $\varepsilon_m'$ and $\varepsilon_d$ are the real part of metal permittivity and dielectric, respectively. As TiN provides a higher negative real part of permittivity compared to Ti,[18,19] the electric field penetration depth into the metal is lower. Thus, hot carriers are generated closer to the MS interface which enhances the probability of hot carrier transfer to a semiconductor. As a result, the proposed arrangement can provide better performances compared to the MIM arrangement with one of the electrodes being Ti.[5] Figures 4 and 5 illustrate the longitudinal

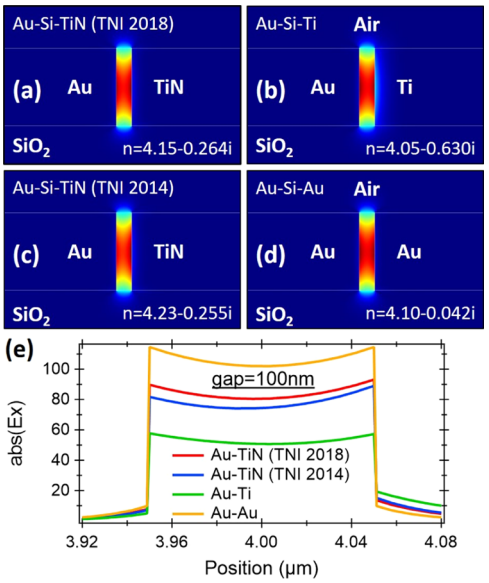


**Figure 4.** Longitudinal component of the electric field inside an Si gap and into the metals for a gap width of $w$ = 100 nm and for different MSM materials: (a) Au−Si−TiN (TNI 2018),[18,19] (b) Au−Si−Ti, (c) Au−Si−TiN (TNI 2014),[18,19] and (d) Au−Si−Au, respectively. The corresponding electric field magnitude as a function of position into the gap and metals, for all the metal combinations, is shown in (e).

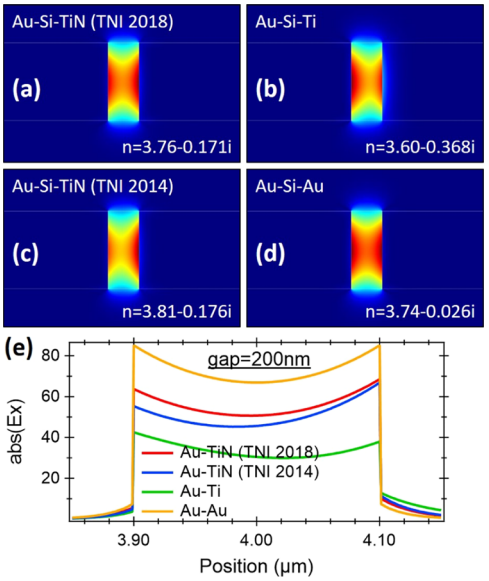


**Figure 5.** Longitudinal component of the electric field inside a Si gap and in the metals for a gap width of $w$ = 200 nm for different MSM materials: (a) Au−Si−TiN (TNI 2018),[18,19] (b) Au−Si−Ti, (c) Au−Si−TiN (TNI 2014),[18,19] and (d) Au−Si−Au, respectively. The corresponding electric field magnitude as a function of position into the gap and metals, for all the metal combinations, is shown in (e).



DOI: 10.1021/acsomega.9b01705
ACS Omega 2019, 4, 17223−17229

component of the electric field inside a Si gap and into the metals for gap widths of $w$ = 100 nm (Figure 4) and $w$ = 200 nm (Figure 5) for different MSM materials: Au−Si−TiN (TNI 2018),[18,19] Au−Si−Ti, Au−Si−TiN (TNI 2014),[18,19] and Au−Si−Au, respectively. The corresponding electric field profile as a function of position, for all the metal combinations, is shown in (i) and (j). This allows for observation of the influence of both material properties and gap width on the electric field's distribution inside the gap, as well as the absorption at the MS interfaces. Figures 6 and 7 show results for the same metal combination but for a wider gap of 500 nm.

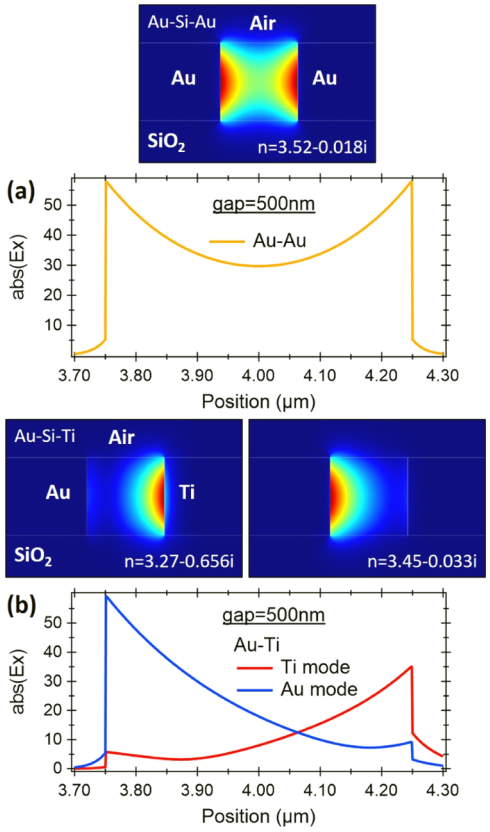


**Figure 6.** Longitudinal component of the electric field inside a Si gap and into the metals for a gap width of $w$ = 500 nm and for the (a) symmetric Au−Si−Au structure and (b) asymmetric Au−Si−Ti structure.

As mentioned in the "Photodetector design" section, the amount of the energy in the metal and dielectric depends on the material's optical properties and the waveguide geometry. A large negative real permittivity of a metal gives small penetration into the metal, whereas a small imaginary permittivity leads to lower losses, hence absorption. The penetration depth into the metal is defined mostly by the longitudinal component of the electric field. For waveguide-integrated PDs, the smaller penetration depth into the metal indicates that more hot carriers can participate in the transition to the semiconductor, enhancing the photocurrent. As the penetration depth in the metal increases, the transition probability decreases. Hot electrons generated far from the MS interface can lose their energy through scattering, which reduces the transition probability to the semiconductor. Thus, for photodetection, the main objective is to achieve high absorption as close as possible to the MS interface.

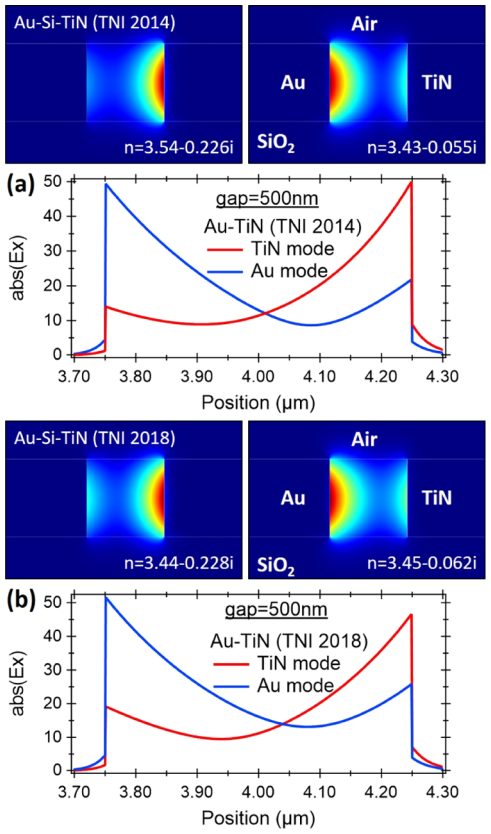


**Figure 7.** Longitudinal component of the electric field inside a Si gap and into the metals for a gap width of $w$ = 500 nm and for asymmetric Au−Si−TiN structures with TiN obtained under slightly different deposition conditions—(a) sample TiN 2014 and (b) sample TiN 2018.[18,19] Corresponding permittivities from refs.[18,19]

For the Au−Si−Au structure, the electric field distribution both in the gap and in the metal is symmetric, which limits its application in a PD. Furthermore, absorption in the metal is very small; thus, a significant amount of hot carriers is not generated. In comparison, the absorption in the metal is highly enhanced when Ti−Si or TiN−Si interfaces are used in Au−Si−Ti or Au−Si−TiN structures, respectively.

The magnitude of the electric field into a MS interface for a gap width of $g$ = 100 nm and for the Ti−Si interface reaches 19.3 (a.u.), while for the TiN−Si interface, it exceeds 15.1 (a.u.) and 13.6 (a.u.). Simultaneously, the absorption depth for Ti is much longer, and even after 50 nm, the magnitude of the electric field into a metal reaches 6.3 (a.u.), while for TiN, this value is achieved only after 25 nm.

As mentioned earlier, hot carriers generated far from the MS interface have a low probability of participating in a transition to a semiconductor. Taking into account an electron mean free path into Ti and TiN that is in the range of 50 nm,[24] we expect a low probability of transition for the hot carriers generated above this distance. It is worth noticing that the imaginary part of the mode effective index for the Au−Si−Ti structure ($n_{im}$ = 0.630·$i$) is more than 2.5 times higher than the imaginary part of the Au−Si−TiN structure ($n_{im}$ = 0.264·$i$ and $n_{im}$ = 0.255·$i$) (Figure 4). Thus, making the Au−Si−TiN PD 2 times longer, we can achieve even better absorption into the metal, and simultaneously, more hot carriers will be generated close to the TiN−Si interface that can participate in a photocurrent generation. As reported in refs,[28,29] the bandwidth of the



DOI: 10.1021/acsomega.9b01705
ACS Omega 2019, 4, 17223−17229

MSM PDs is limited by the carrier transit time rather than by the RC time constant. Thus, making a PD even 2.5 times longer will not influence its bandwidth.

Even more pronounced behavior is observed for the wider gap of $g$ = 200 nm (Figure 5). The magnitude of the electric field at the Ti−Si interface for the Au−Si−Ti structure reaches 12.8 (a.u.) and drops to 4.3 (a.u.) after 50 nm inside Ti. In comparison, the magnitude of the electric field at the TiN−Si interface reaches 11.4 (a.u.) and drops to 2 (a.u.) after the same distance of 50 nm inside TiN. Furthermore, the imaginary part of the mode effective index for the Au−Si−Ti ($n_{im} = 0.368{\cdot}i$) structure is over twice as higher as the Au−Si−TiN structures ($n_{im} = 0.171{\cdot}i$ and $n_{im} = 0.176{\cdot}i$); as a result, a 2 times longer Au−Si−TiN PD can provide the same absorption losses. At the same time, it can ensure much more hot carrier generation in a shorter distance from the MS interface.

When the gap between metals is further increased to $g$ = 500 nm, the absorption losses for the symmetric Au−Si−Au structure decrease as a result of lower electric field penetration into Au (Figure 6a). However, for the asymmetric structures (Figures 6b and 7a,b), it can be observed that two separate modes propagate on each side of the MS interface. For the Au−Si−Ti structure, the real part of the mode effective index for the mode associated with the Au−Si interface is significantly higher than the Ti−Si mode effective index, while the absorption is around 20 times smaller ($n_{eff} = 3.45 - 0.033{\cdot}i$ for Au−Si and $n_{eff} = 3.27 - 0.656{\cdot}i$ for Ti−Si). On the contrary, for the Au−Si−TiN structure, the real part of the mode effective index for both modes associated with the Au−Si and TiN−Si interfaces is very close to each other, with the absorption of mode associated with the TiN−Si interface being 4−5 times higher compared to the mode bounded to the Au−Si interface. Simultaneously, the electric field decays much faster at the TiN−Si interface compared to that at the Ti−Si interface, thus many more hot electrons can participate in a transition to Si.

For the TiN−Si interface, 90% of the power is absorbed within a 33 nm-thick TiN area attached to Si. Compared to it, for the Ti−Si interface, this area increases to 50 nm.[24] Taking into account the electron mean free path in TiN and Ti being evaluated at 50 nm, the hot electron generated in TiN has higher probability to participate in transition to Si without interface scattering compared to Ti. As a result, the internal quantum efficiency increase calculated at 35% can be achieved. Furthermore, compared to Au, Cu, Al, and Ag, TiN provides a lower Fermi energy ($E_F$ = 4.2 eV) and a longer electron mean free path (50 nm). While the former increases the cone of allowed wavevectors of hot electrons that can be injected into the semiconductor, the latter ensures an increase in the number of hot electrons reaching the MS interface. As a result, assuming the Schottky barrier height of $\Phi_B$ = 0.35 eV and Si ($m_s = 0.3{\cdot}m_0$), the probability of IPE of hot electrons generated by a photon with energy $\hbar\omega$ = 0.8 eV ($\lambda$ = 1550 nm) was calculated at 2.4% for Au−Si and 3.2% for TiN−Si. It is over 1.33 times higher for TiN even without taking into account the electron mean free path.

Apart from the responsivity and bandwidth, another important figure of merit of the PD is the signal-to-noise ratio (SNR)[27] defined as SNR = $i_s^2/i_n^2$, where $i_s$ and $i_n$ are the signal and noise currents, respectively. It is highly desired to enhance the signal while keeping the noise at the low level. One solution to achieve a high SNR is by reducing the dimensions of the active Schottky junction area. Another solution is through optimizing the Schottky barrier between the metal and semiconductor that should be as close as possible to the ideal value of ∼0.697 eV for telecom applications at 1550 nm (∼0.8 eV) that is calculated from $\Phi_{Bopt} = h\nu - 4kT/e$.[27] Thus, the Schottky barrier height of $\Phi_B$ = 0.67 eV between TiN and p-doped Si based on our measurements is very close to the optimal value of $\Phi_{Bopt}$ = 0.697 eV for an ideal diode.[27] The Schottky barrier height of $\Phi_B$ = 0.67 eV for the p-Si−TiN contact is much closer to the ideal value when compared to p-Si−Ti or p-Si−Au contacts that were measured at 0.61 and 0.32 eV, respectively.[27]

## CONCLUSIONS

We propose titanium nitride as an alternative material for application in compact waveguide-integrated PDs. In addition to its CMOS compatibility with standard fabrication technology, TiN offers superior electrical properties in terms of the Schottky barrier height, calculated at 0.67 eV for a junction formed between TiN and p-doped Si and 0.35 eV for a junction between TiN and n-doped Si. The value of 0.67 eV is very close to the optimal Schottky barrier height of 0.697 eV for an operating wavelength of 1550 nm (∼0.8 eV) that enables very high SNR. Simultaneously, titanium nitride offers superior optical properties for photodetection—reasonably high negative real part of permittivity and reasonably high imaginary part, enabling a high absorption and reduced penetration depth when compared to Ti. All these properties make titanium nitride a favorable material for the fabrication of on-chip PDs.

## AUTHOR INFORMATION


### Corresponding Author

*E-mail: jg5648@nyu.edu.

### ORCID

Jacek Gosciniak: 0000-0003-2926-9460


### Notes

The authors declare no competing financial interest.

## ACKNOWLEDGMENTS

Support from the NYUAD Research Grant is gratefully acknowledged.

## REFERENCES


(1) Miller, D. A. B. Attojoule Optoelectronics for Low-Energy Information Processing and Communications. *J. Lightwave Technol.* **2017**, *35*, 346−396.

(2) Kimerling, L. C.; Kwong, D.-L.; Wada, K. Scaling computation with silicon photonics. *MRS Bull.* **2014**, *39*, 687−695.

(3) Thomson, D.; Zilkie, A.; Bowers, J. E.; Komljenovic, T.; Reed, G. T.; Vivien, L.; Marris-Morini, D.; Cassan, E.; Virot, L.; Fédéli, J.-M.; Hartmann, J.-M.; Schmid, J. H.; Xu, D.-X.; Boeuf, F.; O'Brien, P.; Mashanovich, G. Z.; Nedeljkovic, M. Roadmap on silicon photonics. *J. Opt.* **2016**, *18*, 073003.

(4) Assefa, S.; Xia, F.; Vlasov, Y. A. Reinventing germanium avalanche photodetector for nanophotonic on-chip interconnects. *Nature* **2010**, *464*, 80−84.

(5) Muehlbrandt, S.; Melikyan, A.; Harter, T.; Köhnle, K.; Muslija, A.; Vincze, P.; Wolf, S.; Jakobs, P.; Fedoryshyn, Y.; Freude, W.; Leuthold, J.; Koos, C.; Kohl, M. Silicon-plasmonic internal-photoemission detector for 40 Gbit/s data reception. *Optica* **2016**, *3*, 741−747.

(6) Goykhman, I.; Sassi, U.; Desiatov, B.; Mazurski, N.; Milana, S.; de Fazio, D.; Eiden, A.; Khurgin, J.; Shappir, J.; Levy, U.; Ferrari, A. C. On-Chip Integrated, Silicon-Graphene Plasmonic Schottky Photo-




DOI: 10.1021/acsomega.9b01705
*ACS Omega* 2019, 4, 17223−17229

detector for High Responsivity and Avalanche Photogain. *Nano Lett.* **2016**, *16*, 3005−3013.
(7) Goykhman, I.; Desiatov, B.; Khurgin, J.; Shappir, J.; Levy, U. Locally Oxidized Silicon Surface-Plasmon Schottky Detector for Telecom Regime. *Nano Lett.* **2011**, *11*, 2219−2224.
(8) Goykhman, I.; Desiatov, B.; Khurgin, J.; Shappir, J.; Levy, U. Waveguide based compact silicon Schottky photodetector with enhanced responsitity in the telecom spectral band. *Opt. Express* **2012**, *20*, 28594.
(9) Gosciniak, J.; Atar, F. B.; Corbett, B.; Rasras, M. Plasmonic Schottky photodetector with metal stripe embedded into semiconductor and with a CMOS-compatible titanium nitride. *Sci. Rep.* **2019**, *9*, 6048.
(10) Othman, N.; Berini, P. Nanoscale Schottky contact surface plasmon "point detectors" for optical beam scanning applications. *Appl. Opt.* **2017**, *56*, 3329−3334.
(11) Spicer, W. E. Photoemissive, Photoconductivite, and Optical Absorption Studies of Alkali-Antimony Compounds. *Phys. Rev.* **1958**, *112*, 114−122.
(12) Spicer, W. E. Negative affinity 3-5 photocathodes: Their physics and technology. *Appl. Phys.* **1977**, *12*, 115−130.
(13) Gramotnev, D. K.; Bozhevolnyi, S. I. Plasmonic beyond the diffraction limit. *Nat. Photonics* **2010**, *4*, 83−91.
(14) Barnes, W. L.; Dereux, A.; Ebbesen, T. W. Surface plasmon subwavelength optics. *Nature* **2003**, *424*, 824−830.
(15) *International Technology Roadmap for Semiconductors 2.0*, 2015
(16) West, P. R.; Ishii, S.; Naik, G. V.; Emani, N. K.; Shalaev, V. M.; Boltasseva, A. Searching for better plasmonic materials. *Laser Photonics Rev.* **2010**, *4*, 795−808.
(17) Naik, G. V.; Shalaev, V. M.; Boltasseva, A. Alternative plasmonic materials beyond gold and silver. *Adv. Mater.* **2013**, *25*, 3264−3294.
(18) Gosciniak, J.; Justice, J.; Khan, U.; Modreanu, M.; Corbett, B. Study of high order plasmonic modes on ceramic nanodisks. *Opt. Express* **2017**, *25*, 5244.
(19) Gosciniak, J.; Justice, J.; Khan, U.; Corbett, B. Study of TiN nanodisks with regard to application for Heat-Assisted Magnetic Recording. *MRS Adv.* **2016**, *1*, 317−326.
(20) Li, W.; Valentine, J. G. Harvesting the loss: surface plasmon-based hot electron photodetection. *Nanophotonics* **2017**, *6*, 177−191.
(21) Chen, T. P.; Lee, T. C.; Ling, C. C.; Beling, C. D.; Fung, S. Current transport and its effect on the determination of the Schottky-barrier height in a typical system: Gold on silicon. *Solid-State Electron.* **1993**, *36*, 949−954.
(22) Harter, T.; Muehlbrandt, S.; Ummethala, S.; Schmid, A.; Nellen, S.; Hahn, L.; Freude, W.; Koos, C. Silicon-plasmonic integrated circuits for terahertz generation and coherent detection. *Nat. Photonics* **2018**, *12*, 625−633.
(23) Naldoni, A.; Guler, U.; Wang, Z.; Marelli, M.; Malara, F.; Meng, X.; Besteiro, L. V.; Govorov, A. O.; Kildishev, A. V.; Boltasseva, A.; Shalaev, V. M. Broadband Hot-Electron Collection for Solar Water Splitting with Plasmonic Titanium Nitride. *Adv. Opt. Mater.* **2017**, *5*, 1601031.
(24) Ishii, S.; Shinde, S. L.; Jevasuwan, W.; Fukata, N.; Nagao, T. Hot Electron Excitation from Titanium Nitride Using Visible Light. *ACS Photonics* **2016**, *3*, 1552−1557.
(25) Scales, C.; Breukelaar, I.; Berini, P. Surface-plasmon Schottky contact detector based on a symmetric metal stripe in silicon. *Opt. Lett.* **2010**, *35*, 529−531.
(26) Akbari, A.; Berini, P. Schottky contact surface-plasmon detector integrated with an asymmetric metal stripe waveguide. *Appl. Phys. Lett.* **2009**, *95*, 021104.
(27) Grajower, M.; Desiatov, B.; Mazurski, N.; Shappir, J.; Khurgin, J. B.; Levy, U. Optimization and experimental demonstration of plasmonic enhanced internal photoemission silicon schottky detectors in the mid-IR. *ACS Photonics* **2017**, *4*, 1015−1020.
(28) Assefa, S.; Xia, F.; Bedell, S. W.; Zhang, Y.; Topuria, T.; Rice, P. M.; Vlasov, Y. A. CMOS-integrated high-speed MSM germanium waveguide photodetector. *Opt. Express* **2010**, *18*, 4986−4999.
(29) Gosciniak, J.; Rasras, M. High-bandwidth and high-responsivity waveguide-integrated plasmonic germanium photodetector. *J. Opt. Soc. Am. B* **2019**, *36*, 2481−2491.
(30) Grajower, M.; Levy, U.; Khurgin, J. B. The Role of Surface Roughness in Plasmonic-Assisted Internal Photoemission Schottky Photodetectors. *ACS Photonics* **2018**, *5*, 4030−4036.



DOI: 10.1021/acsomega.9b01705
*ACS Omega* 2019, 4, 17223−17229